Precision Engineering 33 (2009) 26–36

Contents lists available at ScienceDirect

Precision Engineering

journal homepage: www.elsevier.com/locate/precision

An improved tool–holder model for RCSA tool-point frequency response prediction

S. Filiz[a], C.-H. Cheng[b], K.B. Powell[b], T.L. Schmitz[b], O.B. Ozdoganlar[a,*]

[a] Department of Mechanical Engineering, Carnegie Mellon University, Pittsburgh, PA 15213-3890, United States
[b] Department of Mechanical and Aerospace Engineering, University of Florida, Gainesville, FL 32611, United States

ARTICLE INFO

Article history:
Received 17 January 2007
Received in revised form 20 February 2008
Accepted 11 March 2008
Available online 4 April 2008

Keywords:
Machine-tool dynamics
Machining stability
Milling
Chatter
Receptance coupling

ABSTRACT

In addition to the precise kinematic motions of the machine tools and spindles, machining accurate parts necessitates controlling the dynamic behavior of the tool tip with respect to the workpiece. High-fidelity models of tool-tip dynamics can be used to select operating parameters that improve the accuracy by reducing the effect of vibrations. To effectively model the tool-tip dynamics for arbitrary tool-and-holder combinations using the receptance coupling substructure analysis (RCSA) technique, highly accurate and numerically efficient models of the tool–holder dynamics are needed. In this paper, we present a tool–holder model that incorporates a spectral-Tchebychev technique with the Timoshenko beam equation to obtain a completely parameterized solution. Comparison of the tool–holder model to a three-dimensional finite elements solution shows that the dynamic behavior is captured with sufficient accuracy. The tool–holder model is then coupled with the experimentally determined spindle–machine dynamics through RCSA to realize a model of the tool-tip dynamics. The coupled model is validated through experiments for three different tool overhang lengths. The presented technique can be used to predict the tool-tip dynamics for different tool-and-holder combinations and for optimization studies without the need for extensive experimentation.

1. Introduction

It is well-established in literature that the dynamic behavior of the tool–holder–spindle–machine assembly, as reflected at the tool tip, plays a significant role in determining the precision of machining processes [1–6]. The process efficiency can also be limited due to the dynamic motions of the tool tip. These limitations include unstable cutting conditions (chatter) caused by regeneration of waviness, or the over-cutting of the surface left by one tooth of the vibrating cutter by subsequent teeth. It has been shown that the limiting axial depth of cut is directly dependent on the tool-point dynamic response [7–12]. Similarly, even under stable cutting conditions, forced vibrations of the flexible tool can lead to errors in the location of the machined surface [1,2,4,5,13,14]. Again, the magnitude of these errors depends on the tool-point dynamic response. In both cases, if the dynamic response is known, models can be applied to select preferred cutting conditions (spindle speed, depths of cut, and feed rate) for increased stability and reduced surface location error. Therefore, a method to predict the assembly frequency response using a minimum number of measurements is desired, particularly in situations where a number of different tool–holder–spindle–machine combinations are available.

To illustrate the importance of considering surface location error (during stable machining), Canning et al. [15] completed a study to quantify the relative contributions of geometric, thermal, contouring, and cutting force errors to machined part dimensional errors on a high-speed computer numerically controlled machining center. Measurements were performed to independently evaluate the: (1) quasi-static geometric errors using the laser ball bar [16]; (2) variations in geometric errors due to thermal effects; (3) spindle thermal growth errors using a capacitance gage nest; (4) two-dimensional contouring errors using a grid plate encoder; and (5) surface location error, or SLE. The results are provided in Fig. 1 for a selected tool–holder combination, where the individual contribution levels (worst case) were: 6 μm for spindle thermal growth; 17 μm for geometric/contouring; and 70 μm for SLE. Clearly, the spindle speed-dependent SLE is an important error contributor. This highlights the usefulness of an accurate model capable of predicting the tool-point dynamic behavior so that spindle speeds that exhibit small surface location error can be selected a *priori* through milling process models.

The interaction between the machine, spindle, tool–holder, and tool dynamics influence the overall dynamic behavior of the system. To predict the assembly behavior in the presence of changing

* Corresponding author.
E-mail address: ozdoganlar@cmu.edu (O.B. Ozdoganlar).

0141-6359/$ – see front matter © 2008 Elsevier Inc. All rights reserved.
doi:10.1016/j.precisioneng.2008.03.003

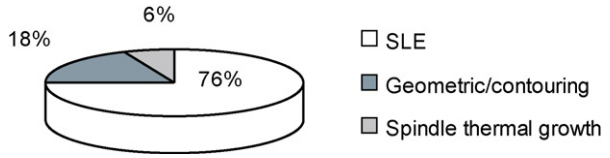

Fig. 1. Percent contribution of error sources to workpiece accuracy from Canning et al. [15] study.

system components (i.e., different tool–holders, endmills, etc.), a receptance coupling substructure analysis (RCSA) method was developed by Schmitz et al. [17–21]. This method enabled prediction of the dynamic behavior at the tool tip by combining the spindle–machine dynamics and tool–holder dynamics in the frequency domain. Since accurate models of the dynamics of the spindle–machine portion (including its energy dissipation behavior) are not generally available, impact testing was used to describe its dynamic behavior in the form of complex receptances.

The tool–holder portion, on the other hand, was modeled using Euler–Bernoulli (E–B) and Timoshenko beam models with constant cross-sections [22–25]. At each discontinuity in the tool–holder cylindrical geometry, a new free-free beam was defined. For tapered sections (common to thermal shrink-fit tool–holders), the taper was approximated as a number of constant diameter sections (the straight beam assumption). The full collection of free-free beams was then coupled using RCSA. This result was finally coupled to the spindle–machine receptances. While reasonable agreement with experiments was obtained, the Euler–Bernoulli models suffer from the well-known natural frequency errors for stubby (non-slender) beams due to the neglected shear effects. Although the Timoshenko beam model incorporates shear effects and predicts the natural frequencies and mode shapes more accurately, its numerical solution (through finite elements method) was cumbersome to implement in an otherwise analytical approach. Furthermore, it was necessary to repeat the numerical solution for each change in the model (e.g., tool overhang length, tool diameter, and holder design). As such, an improved model of the tool–holder assembly with increased accuracy and numerical efficiency is needed for predicting the tool-tip dynamics for different tool-and-holder combinations, particularly for conducting optimization studies. The purpose of this paper is to extend the prior RCSA tool-point frequency prediction efforts [17–21] through an improved tool–holder modeling technique. The RCSA method is composed of four fundamental steps: (1) a standard geometry artifact is inserted in the spindle and direct and cross frequency response functions (FRFs) are recorded by impact testing; (2) the portion of the standard artifact beyond the flange is removed in simulation (inverse RCSA or decomposition) to isolate the spindle–machine response; (3) a model of the desired tool–holder is developed; and (4) the FRF of the model is coupled to the spindle–machine FRF.

In this work, a new method for the tool–holder model (defined in step (3) above) is described. This method uses Timoshenko beam equations to model the complete tool–holder, including the actual tapered geometry. A novel spectral-Tchebychev technique is used for simplified, numerically efficient solution of the boundary-value problem. This technique allows different tool–holder geometries to be modeled without the need for re-derivation of the solution. The accuracy of different modeling techniques using Euler–Bernoulli and Timoshenko beam models is assessed by comparing the natural frequencies and mode shapes to those from a three-dimensional finite elements solution. The validity of approximating the tapered geometry with equivalent straight beams is also evaluated. The developed model is then coupled to the spindle–machine dynamics through RCSA and the results are validated through experimentation for three different tool overhang lengths.

2. Receptance coupling substructure analysis (RCSA) method

A brief review of the three-component RCSA model from [18] is provided in this section. Consider the tool–holder and spindle–machine assembly shown in Fig. 2. First, a standard artifact is inserted in the spindle (in place of the tool–holder) and a set of modal tests are conducted. An inverse RCSA procedure is then conducted to remove the effect of the standard artifact and thus to isolate the spindle–machine receptances G_{33} [18]. Second, the free-free response of the tool–holder portion is obtained from a model. The corresponding RCSA equation for the assembly receptances at the tool-point is obtained by:

(1) determining the free-free tool–holder direct receptances G_{11} and G_{22}, and the cross receptances G_{12} and G_{21} at each end, where

$$G_{ij} = \begin{bmatrix} \frac{x_i}{f_j} & \frac{x_i}{m_j} \\ \frac{\theta_i}{f_j} & \frac{\theta_i}{f_j} \end{bmatrix} \quad (1)$$

describes the subassembly FRFs for displacements x_i and rotations θ_j in response to applied moments m_j and forces f_j;

(2) coupling these receptances to the direct receptances G_{33} at the free end of the spindle–machine subassembly as

$$\begin{bmatrix} H_{11} & L_{11} \\ N_{11} & P_{11} \end{bmatrix} = G_{11} - G_{12}(G_{22} + G_{33})^{-1} G_{21}. \quad (2)$$

In this equation, $H_{11}(\omega) = (X_1/F_1)$ is the assembly FRF required for milling stability and surface location error analysis, where X_1 is the lateral translation at assembly coordinate 1 and F_1 is a harmonic force applied at coordinate 1; $L_{11}(\omega) = (X_1/M_1)$ describes the displacement at coordinate 1 due to a unit moment M_1 applied at coordinate 1; and $N_{11}(\omega)(\Theta_1/F_1)$ describes the angular motion Θ_1 at coordinate 1 due to the force F_1; and $P_{11}(\omega) = (\Theta_1/M_1)$ describes the rotation at coordinate 1 due to the moment applied at coordinate 1.

3. Tool–holder model using the spectral-Tchebychev technique

Cutting tools and tool–holders used in milling operations are generally characterized by non-slender geometries. For such stubby structures, the shear effects on dynamic behavior become more prominent and the commonly used Euler–Bernoulli beam models are less effective. In this work, the tool–holder assembly is modeled using the Timoshenko beam equations to incorporate the shear effects.

Although obtaining the Timoshenko beam equations is straightforward, solving these equations poses considerable challenges.

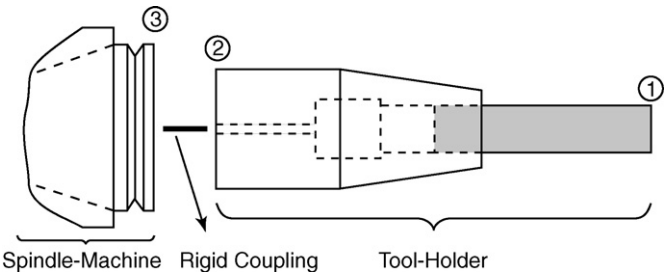

Fig. 2. Three-component RCSA model—example coordinate definitions.

Since an analytical solution of the associated eigenvalue problem does not exist, normal-mode expansion (mode summation) procedure cannot be directly applied. This section introduces a new approach, *the spectral-Tchebychev* technique, for solving the Timoshenko beam equations including varying cross-sectional geometry, such as the tapered section of a shrink-fit tool–holder. To reduce the numerical inefficiencies arising from discontinuities, the sections of the tool–holder assembly with different geometric and material properties are modeled individually [26]; and a component-mode synthesis technique is applied to analytically combine those models. Lastly, the solution is transformed from the time domain to frequency domain to allow its usage with RCSA.

3.1. Tchebychev polynomials and Tchebychev expansion

Tchebychev polynomials are a set of recursive orthogonal polynomials that can be described as

$$\bar{T}_k(x) = \cos(k\,\cos^{-1}(x)) \quad \text{for } k = 0 \ldots \infty, \tag{3}$$

where k is an integer. Although defined for all x values, Tchebychev polynomials are a stable representation only on the $(-1, 1)$ interval. In this interval, they form a complete set, which means that any function $y(x)$ can be represented by a series expansion using Tchebychev polynomials. Since in beam problems the physical dimension along the length of the beam is on the interval $(0, L)$, a mapping (scaling) between $(0, L)$ to $(-1, 1)$ is first applied to shift the domain of the polynomials. The scaled Tchebychev polynomials will be denoted as $T_k(x)$. First six Tchebychev polynomials are plotted in Fig. 3. Consider a function $y(x)$ in the domain $0 \le x \le 1$. This function can be expressed using a Tchebychev series expansion as

$$y(x) = \sum_{k=1}^{\infty} a_k T_{k-1}(x). \tag{4}$$

Since for any square-integrable function, the Tchebychev expansion converges exponentially [27], an N-term representation can represent the function with sufficient accuracy. Therefore, a function $y(x, t)$ can be represented in the Tchebychev space with an N-vector $\underline{a}\{a_k\}$.

It can be shown that the Tchebychev coefficients $\underline{a}$ can be determined from

$$\underline{a} = \Gamma_F \underline{y}, \tag{5}$$

where $\underline{y}$ is obtained by sampling the continuous function $y(x)$ at certain intervals, and Γ_F is the forward transformation matrix. This relationship can also be expressed as

$$\underline{y} = \Gamma_B \underline{a}, \tag{6}$$

where $\Gamma_B = \Gamma_F^{-1}$ is the backward transformation matrix.

Another important property of the Tchebychev expansions is that the derivatives of the Tchebychev polynomials can be expressed as a linear combination of lower-order Tchebychev polynomials. Therefore, if the Tchebychev expansion of n th derivative of $y(x)$ is given as

$$y^{(n)}(x) = \sum_{k=1}^{N} a_k^{(n)} T_{k-1}(x), \tag{7}$$

then a relationship between $\underline{a}^n$ and $\underline{a}$ can be written as

$$\underline{a}^n = D^n \underline{a}, \tag{8}$$

where D is the derivative matrix. Using the forward and backward transformations, this expression can be represented in the physical (sampled) domain as

$$\underline{y}^{(n)} = Q_n \underline{y}, \quad \text{where } Q_n = \Gamma_B D^n \Gamma_F, \tag{9}$$

and Q_n is referred to as the n th derivative matrix. If the N-term Tchebychev expansion describes the function $y(x)$ exactly, than $y^{(n)}(x)$ obtained from Eq. (9) will be exact.

Similarly, the inner product of two functions that are expressed by Tchebychev expansion can be written as

$$\int_{x=0}^{x=1} y(x) z(x)\,\mathrm{d}x = \underline{y}^{\mathrm{T}} V \underline{z}, \tag{10}$$

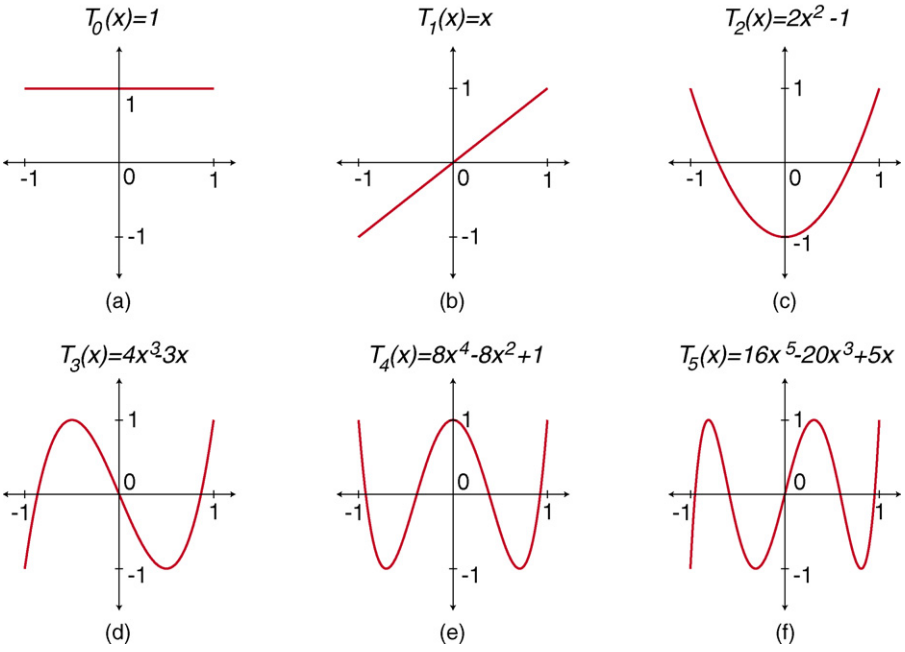

Fig. 3. Plots and polynomial representations of first six Tchebyshev polynomials between $(-1, 1)$.

where V is the inner product matrix and the superscript 'T' indicates transpose. If the N-term expansion of functions y and z are exact, then this inner product is calculated exactly.

It should be noted that the matrices D and V are known. In addition, for a specific sampling scheme, Γ_F and Γ_B can be determined. The forward and backward transformation matrices assume simpler forms if the sampling is performed at the Gauss–Lobatto points [27].

3.2. The spectral-Tchebychev technique for the Timoshenko beam model

A non-dimensional form of the Timoshenko beam equations can be written as

$$y'' - \psi' - \chi\ddot{y} = \gamma f(x,t), \quad 0 < x < 1, \tag{11}$$

$$\frac{1}{\sigma}\psi'' + (y' - \psi) - \frac{\mu}{\sigma}\ddot{\psi} = \frac{\eta}{\sigma}\Psi(x,t), \quad 0 < x < 1, \tag{12}$$

where $y(x,t)$ is the flexural displacement, $\psi(x,y)$ is the slope, $f(x,t)$ is the applied force, and $\Psi(x,t)$ is the applied moment. The constants used in this equation can be given as

$$\chi = \frac{mL^2\omega^2}{k'GA}, \qquad \mu = \frac{J\omega^2L^2}{EI}, \qquad \gamma = \frac{-L}{k'GA},$$
$$\sigma = \frac{k'GAL^2}{EI}, \qquad \eta = \frac{-L^2}{EI}, \tag{13}$$

where m is the mass per unit length, L is the length of the beam, ω is the reference frequency for nondimensionalizing the time, k' is the shear factor, G is the shear modulus, A is the cross-sectional area, J is the polar moment of inertia, E is Young's modulus, and I is the area moment of inertia in bending.

The generic boundary conditions, which are assumed to be linear for the following derivation, are given as

$$B_{yij}y + B_{\psi ij}\psi = \alpha(t), \quad \text{for } i = 0, 1 \text{ and } j = 1, 2, \tag{14}$$

where B_y and B_ϕ are differential operators for displacement and slope, respectively, $\alpha(t)$ is the time-dependent right-hand side of the boundary conditions, and i represents the two boundaries (ends) of the beam. For each end, two boundary conditions ($j = 1, 2$) must be satisfied.

The spectral-Tchebychev method that will be used to solve the Timoshenko beam equations is based on describing the flexural displacement and slope using Tchebychev series expansion as

$$y(x,t) = \sum_{k=1}^{N} a_k(t)T_{k-1}(x), \qquad \psi(x,t) = \sum_{k=1}^{N} b_k(t)T_{k-1}(x), \tag{15}$$

where a_k and b_k are the k th coefficients of the Tchebychev expansion, and $T_k(x)$ is the k th (scaled) Tchebychev polynomial. Using Tchebychev expansion, the sampled version of the boundary value problem can be given as

$$Q_2\underline{y} - Q_1\underline{\psi} - \chi\underline{\ddot{y}} = \gamma\underline{f}, \tag{16}$$

$$\frac{1}{\sigma}Q_2\underline{\psi} + (Q_1\underline{y} - \underline{\psi}) - \frac{\mu}{\sigma}\underline{\ddot{\psi}} = \frac{\eta}{\sigma}\underline{\Psi}, \tag{17}$$

subjected to boundary conditions

$$\underline{e}_1^T(\bar{B}_{yj}\underline{y} + \bar{B}_{\psi j}\underline{\psi}) = \alpha_{0j}, \quad j = 1, 2,$$
$$\underline{e}_N^T(\bar{B}_{yj}\underline{y} + \bar{B}_{\psi j}\underline{\psi}) = \alpha_{1j}, \quad j = 1, 2,$$

where Q_n is defined in Eq. (9), $\underline{f}$ is the spatially discretized version of $f(x,t)$, and $\bar{B}$ is the (matrix) boundary operator in the Tchebychev space corresponding to the differential boundary operator B_{ij}. Here it was assumed that the same number of polynomials (N) were used to express both y and ψ. The subscript p of $\underline{e}_p$ prescribes the location of the boundary, where $p = 1$ indicates $x = 0$ and $p = N$ indicates $x = 1$. The p th element of the vector $\underline{e}_p$ is unity, and all other elements are zeros.

The solution of Eqs. (16) and (17) will be obtained by using the weighted-residuals method. In this approach the residues associated with Eqs. (16) and (17) are defined as

$$\underline{\theta}_y = Q_2\underline{y} - Q_1\underline{\psi} - \chi\underline{\ddot{y}} - \gamma\underline{f}, \tag{18}$$

$$\underline{\theta}_\psi = \frac{1}{\sigma}Q_2\underline{\psi} + (Q_1\underline{y} - \underline{\psi}) - \frac{\mu}{\sigma}\underline{\ddot{\psi}} - \frac{\eta}{\sigma}\underline{\Psi}. \tag{19}$$

It is then required that the inner product of the residues with arbitrary weighting functions ϕ vanishes, viz.,

$$\int_0^L \phi_y(x)\theta_y(x)\,dx = 0, \qquad \int_0^L \phi_\psi(x)\theta_\psi(x)\,dx = 0. \tag{20}$$

From Eq. (10), these inner products can be written in the Tchebychev space as

$$\int_0^L \phi_y(x)\theta_y(x)\,dx = \underline{\phi}_y^T V\underline{\theta}_y, \qquad \int_0^L \phi_\psi(x)\theta_\psi(x)\,dx = \underline{\phi}_\psi^T V\underline{\theta}_\psi. \tag{21}$$

Substituting $\underline{\theta}_y$ and $\underline{\theta}_\psi$, we obtain

$$\underline{\phi}_y^T[V((Q_2\underline{y} - Q_1\underline{\psi}) - \chi\underline{\ddot{y}} - \gamma\underline{f})] = 0, \tag{22}$$

$$\underline{\phi}_\psi^T\left[V\left(\frac{1}{\sigma}Q_2\underline{\psi} + (Q_1\underline{y} - \underline{\psi}) - \frac{\mu}{\sigma}\underline{\ddot{\psi}} - \frac{\eta}{\sigma}\underline{\Psi}\right)\right] = 0. \tag{23}$$

Defining,

$$\underline{q} = \begin{bmatrix}\underline{y}\\ \underline{\psi}\end{bmatrix}, \qquad \underline{\phi} = \begin{bmatrix}\underline{\phi}_y\\ \underline{\phi}_\psi\end{bmatrix}, \qquad V_s = \begin{bmatrix}V & 0\\ 0 & V\end{bmatrix}, \qquad F = \begin{bmatrix}\underline{f}\\ \underline{\Psi}\end{bmatrix}, \tag{24}$$

the boundary-value problem can be written as

$$\underline{\phi}^T V_s(M_s\underline{\ddot{q}} + K_s\underline{q} - B_s\underline{F})\underline{0}, \tag{25}$$

where

$$M_s = \begin{bmatrix}-\chi\Pi & 0\\ 0 & \frac{-\mu}{\sigma}\Pi\end{bmatrix}, \qquad K_s = \begin{bmatrix}Q_2 & -Q_1\\ Q_1 & \frac{1}{\sigma}Q_2 - \Pi\end{bmatrix},$$
$$B_s = \begin{bmatrix}\gamma\Pi & 0\\ 0 & \frac{\eta}{\sigma}\Pi\end{bmatrix}, \tag{26}$$

and Π indicates the identity matrix. An effective way of imposing the boundary condition is to express $\underline{y}$ using projection matrices (basis recombination) as

$$\underline{q} = P\underline{z} + R\underline{\alpha}, \tag{27}$$

where, for M boundary conditions, P and R are $2N \times (2N - M)$ and $2N \times M$ projection matrices, respectively, and $\underline{z}$ is an $(2N - M)$ vector. Numerically, the P and R matrices are determined through singular-value decomposition.

A special case of the weighted residuals method (commonly referred to as *Galerkin's method*) can be realized by requiring the weighting functions $\underline{\phi}$ to be from the admissible functions, i.e., those that satisfy the geometric (homogeneous) boundary conditions. Considering the projection matrices above, such weighting functions can be expressed as $\underline{\phi} = P\underline{\bar{\phi}}$. Thus, Eq. (25) becomes

$$\underline{\bar{\phi}}^T P^T V_s(M_s(P\underline{\ddot{z}} + R\underline{\ddot{\alpha}}) + K_s(P\underline{z} + R\underline{\alpha}) - B_s\underline{F}) = \underline{0}. \tag{28}$$

Since these equations must be satisfied for arbitrary $\underline{\bar{\phi}}$,

$$P^T V_s M_s P\underline{\ddot{z}} + P^T V_s K_s P\underline{z} = P^T V_s B_s\underline{F} - P^T V_s M_s R\underline{\ddot{\alpha}} - P^T V_s K_s R\underline{\alpha}. \tag{29}$$

This equation is in the general form of

$$M\underline{\ddot{z}} + K\underline{z} = F, \tag{30}$$

which can be numerically integrated using the state-space approach.

It is important to note here that for a self-adjoint system such as that in Eqs. (11) and (12), the system matrices obtained through the spectral-Tchebychev technique are symmetric. The symmetry is critical for numerical stability of the solution.

3.3. Spatially varying parameters

In the preceding derivation, the parameters were considered as constants with respect to the spatial variable x. However, some parameters such as m (and thus χ in Eq. (11)) and I vary spatially along various sections of the tool–holder assembly. The application of the spectral-Tchebychev technique must be generalized to handle such geometry variations.

For instance, consider χ in Eq. (11) to vary spatially, i.e., $\chi = \chi(x)$. The component $\chi(x)\ddot{y}$ of Eq. (18) will be evaluated in the inner product (Eq. (21)) as

$$\int_0^L \phi_y(x)\,\chi(x)\,\ddot{y}(x)\,\mathrm{d}x = \underline{\phi_y}^{\mathrm{T}} V_\chi\, \underline{\ddot{y}}, \tag{31}$$

where V_χ is a symmetric matrix that includes the spatial variation associated with χ. Accordingly, Eqs. (22) and (25) are rewritten as

$$\underline{\phi_y}^{\mathrm{T}}[V(Q_2\underline{y} - Q_1\underline{\psi}) - V_\chi\,\underline{\ddot{y}} - \gamma V\underline{f}] = 0, \tag{32}$$

$$\underline{\phi}^{\mathrm{T}}(M_{s\chi}\underline{\ddot{q}} + V_s K_s \underline{q} - V_s B_s \underline{F}) = \underline{0}, \tag{33}$$

respectively, where

$$M_{s\chi} = \begin{bmatrix} -V_\chi & 0 \\ 0 & \dfrac{-\mu}{\sigma}\Pi \end{bmatrix}. \tag{34}$$

These changes are reflected in the $\underline{\ddot{y}}$ and $\underline{\ddot{\alpha}}$ components of Eq. (29) as

$$P^{\mathrm{T}} M_{s\chi} P\,\underline{\ddot{z}} \quad \text{and} \quad P^{\mathrm{T}} M_{s\chi} R\,\underline{\ddot{\alpha}}, \tag{35}$$

respectively.

3.4. Component mode synthesis

Discontinuities in geometric and material parameters can considerably reduce the numerical efficiency of spectral solutions. To ensure the numerical efficiency and accuracy of the tool–holder model in the presence of discontinuities, the tool–holder geometry will be divided into individual continuous sections as shown in Fig. 4. The complete model will be realized by connecting the sections through a component mode synthesis technique.

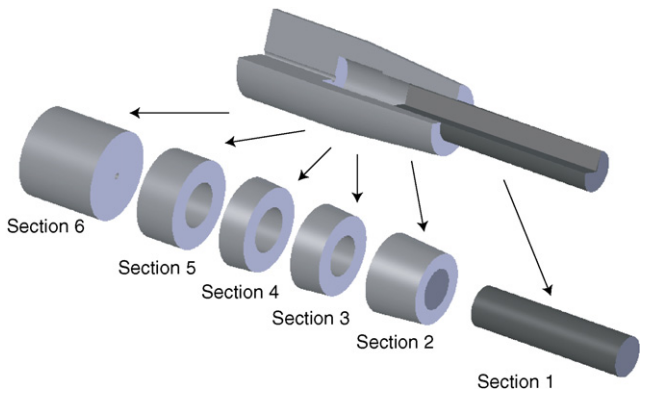

Fig. 4. Sections of the tool–holder assembly.

For each section, the boundary-value problem is formulated using a separate set of Tchebychev polynomials, resulting in different deflection vectors ($\underline{q}$), inner product matrices (V_s), and derivative matrices (Q_n). Considering the compatibility conditions (equivalency of displacements, slopes, forces and moments) at common section boundaries, the global boundary conditions and global mass, stiffness and forcing matrices are then obtained. Using the global boundary conditions matrix, the projection matrices are written as

$$\underline{q}_{\mathrm{G}} = P_{\mathrm{G}}\,\underline{z}_{\mathrm{G}} + R_{\mathrm{G}}\,\underline{\alpha}_{\mathrm{G}}, \tag{36}$$

where $\underline{q}_{\mathrm{G}}$ is the global deflections and slopes including those of each sections, P_{G} and R_{G} are the global projection matrices, and α_{G} is the global (combined) non-homogenous part of the boundary conditions (such as external forces).

Following the same procedure as before, and composing the global mass and stiffness matrices, the system equation (corresponding to Eq. (29)) is written as

$$P_{\mathrm{G}}^{\mathrm{T}} M_{\mathrm{G}} P_{\mathrm{G}}\,\underline{\ddot{z}} + P_{\mathrm{G}}^{\mathrm{T}} K_{\mathrm{G}} P_{\mathrm{G}}\,\underline{z} = P_{\mathrm{G}}^{\mathrm{T}} B_{\mathrm{G}}\,\underline{F} - P_{\mathrm{G}}^{\mathrm{T}} M_{\mathrm{G}} R_{\mathrm{G}}\,\underline{\ddot{\alpha}} - P_{\mathrm{G}}^{\mathrm{T}} K_{\mathrm{G}} R_{\mathrm{G}}\,\underline{\alpha}. \tag{37}$$

3.5. Frequency-domain solution

In order to couple the model-based solution of the tool–holder dynamics with the experimentally determined spindle–machine dynamics through the RCSA technique, the dynamics of the tool–holder assembly must be represented in the frequency domain. The frequency-domain solution (i.e., the FRF) of the tool–holder dynamics will be obtained from the time-domain discretized differential equation presented in Eq. (37).

Since the RCSA technique requires the receptances only at the section ends, in deriving the FRF from the model the distributed force F in Eq. (37) will be set to zero. Instead, a unit force (and moment) will be considered at the section boundaries through a non-zero $\underline{\alpha}$ utilizing force (and moment) boundary conditions. Taking the Laplace transform of both sides of Eq. (37) with $\underline{F} = \underline{0}$ yields,

$$(m_z s^2 + k_z)\underline{Z}(s) = -(m_\alpha s^2 + k_\alpha)\underline{\alpha}(s), \tag{38}$$

where $\underline{Z}(s)$ and $\underline{\alpha}(s)$ are the Laplace domain variables corresponding $\underline{z}(t)$ and $\underline{\alpha}(t)$, and

$$m_z = P_{\mathrm{G}}^{\mathrm{T}} M_{\mathrm{G}} P_{\mathrm{G}}, \qquad k_z = P_{\mathrm{G}}^{\mathrm{T}} K_{\mathrm{G}} P_{\mathrm{G}}, \qquad m_\alpha = P_{\mathrm{G}}^{\mathrm{T}} M_{\mathrm{G}} R_{\mathrm{G}},$$
$$k_\alpha = P_{\mathrm{G}}^{\mathrm{T}} K_{\mathrm{G}} R_{\mathrm{G}}. \tag{39}$$

Writing $\underline{Q}(s) = P\,\underline{Z}(s) + R\,\underline{\alpha}(s)$ from Eq. (27) and substituting this into Eq. (38), after manipulation, we obtain

$$\underline{Q}(s) = [-P(m_z s^2 + k_z)^{-1}(m_\alpha s^2 + k_\alpha) + R]\,\underline{\alpha}(s). \tag{40}$$

Therefore, the transfer matrix can be written as

$$G(s) = [-P(m_z s^2 + k_z)^{-1}(m_\alpha s^2 + k_\alpha) + R].$$

The frequency response matrix can then be obtained by substituting $s = \mathrm{j}\omega$ into this equation as

$$G(\mathrm{j}\omega) = -P[m_z(\mathrm{j}\omega)^2 + k_z]^{-1}[m_\alpha(\mathrm{j}\omega)^2 + k_\alpha] + R. \tag{41}$$

The frequency response matrix in Eq. (41) includes FRFs between the boundaries of each sections of the tool–holder. The required direct and cross receptances from the two ends of the tool–holder (G_{11}, G_{12}, G_{21}, and G_{22} in Eq. 2) can be extracted from Eq. (41) by selecting rows and columns associated with each end of the tool–holder.

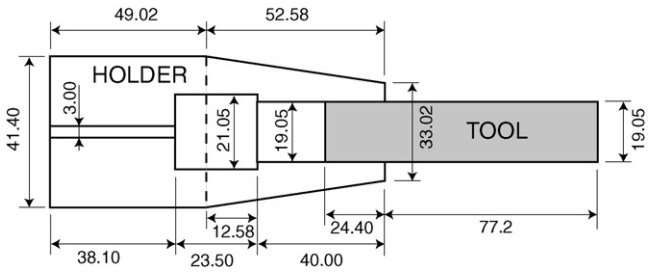

Fig. 5. The geometric dimensions (in mm) of tool–holder used during modeling and experimental validation.

4. Comparison of tool–holder modeling techniques

In this section, the accuracy of different modeling techniques are assessed. The purpose of this assessment is to provide a guideline in striking the tradeoff between solution accuracy and the computational burden associated with the solution.

4.1. Euler–Bernoulli, Timoshenko, and FEM solutions

Due to its simplicity, the Euler–Bernoulli beam equation is commonly used to model beams, such as those of the individual sections of the tool–holder in Fig. 4. It is well known, however, that as the length-to-diameter ratio reduces, the shear effects become increasingly more important, and the Euler–Bernoulli solution become progressively less accurate. In those cases, the Timoshenko beam equation that incorporates the shear effects is applied. However, the Timoshenko beam solution adds considerable complexity since a closed-form solution of the associated eigenvalue problem does not exist and, thus, the normal-mode summation cannot be directly used. The spectral-Tchebychev technique described previously can be applied to solve the Euler–Bernoulli and Timoshenko beam equations in the presence of varying geometric parameters.

In this section, comparison between the use of Euler–Bernoulli and Timoshenko beam equation in solving the tool–holder assembly dynamics is presented. The geometric dimensions of the tool–holder used during this comparison are given in Fig. 5. Table 1 provides the material properties for the steel holder and carbide tool. The solutions are compared to those from a three-dimensional finite elements model (FEM) solution obtained using `Solid 187` tetrahedral structural solid elements in ANSYS® Version 10. The comparisons were made in terms of the natural frequencies and mode shapes for both free-free and fixed-free boundary conditions.

The FEM model of the tool–holder assembly is shown in Fig. 6. A convergence study was completed for the FEM solution by incrementally increasing the mesh density and comparing the first five natural frequencies. The appropriate mesh density was selected when the change in natural frequencies was reduced to below 0.25%, resulting in 55,245 elements.

A similar convergence study was required for the spectral-Tchebychev solution. For each of the Euler–Bernoulli and Timoshenko-based solutions, the number of polynomials used for each sections of the tool–holder assembly was increased from eight,

Table 1
Material properties of the tool (carbide) and the holder (steel)

	Steel	Carbide
Young's modulus, E (GPa)	200	550
Density, ρ (kg/m^3)	7850	14500
Poisson's ratio, ν	0.29	0.22

and the relative differences (ϵ) between each of the first five natural frequencies were calculated as

$$\epsilon_N\ (\%) = \frac{|\omega_N - \omega_N - 1|}{\omega_N} \times 100,$$

where ω_N is the natural frequency calculated while using N polynomials for each section. The relative difference reached a value of less than 1×10^{-10} when the polynomial number was increased to 14. Accordingly, 14 polynomials were selected to model each section of the tool–holder assembly.

Fig. 7(a) provides the magnitude of the driving-point frequency response functions (receptances) of the tool–holder assembly model from the tool tip using the Euler–Bernoulli and Timoshenko beam models for free-free boundary conditions. The natural frequencies obtained from the FEM solution are also indicated with dashed vertical lines. Fig. 7(b) gives the same plots for the fixed-free boundary conditions. The beam solutions were obtained using the spectral-Tchebychev technique described above, and modal damping ratios less than 0.1% were considered. Table 2 lists the resulting natural frequencies for the first four bending modes. The difference between the FEM solution and each of the E–B and Timoshenko solutions are given in parenthesis as a percentage. Fig. 8 gives the mode shapes of E–B and Timoshenko solutions for both free-free and fixed-free boundary conditions.

It is seen from Fig. 7(a) and (b) and Table 2 that the Timoshenko beam model produces natural frequencies that are very close to those from the FEM model. For the free-free boundary condition, the largest error of the Timoshenko beam model is 6.3%, which is seen for the first mode. This error is attributed to the fact that some of the sections of the tool–holder assembly (such as Sections 3 and 4) are too stubby to be modeled as beams. The maximum error reduces to 3.7% for the case of the fixed-free boundary conditions. Since the fixed-free model reflects the behavior of the tool–holder within the tool-tip dynamics response [18] more closely, the tool–holder model can be considered sufficiently accurate.

Fig. 7(a) and (b), Table 2, and Fig. 8 show that the E–B solution results in large errors in natural frequencies and mode shapes, especially at higher modes. The difference between the mode shapes of the E–B and Timoshenko solutions are quantified by calculating a norm as

$$\epsilon_r\ (\%) = \frac{\int_0^L |r_E(x) - r_T(x)|\,dx}{\int_0^L |r_T(x)|\,dx} \times 100, \quad (42)$$

where r_E and r_T are the mode shapes from the E–B and Timoshenko solutions, respectively, and L is the length of the tool–holder assembly. The difference between the first four mode shapes

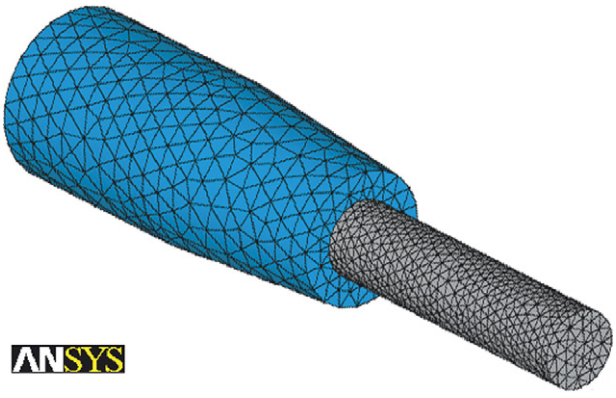

Fig. 6. The three-dimensional finite elements model of the tool–holder.

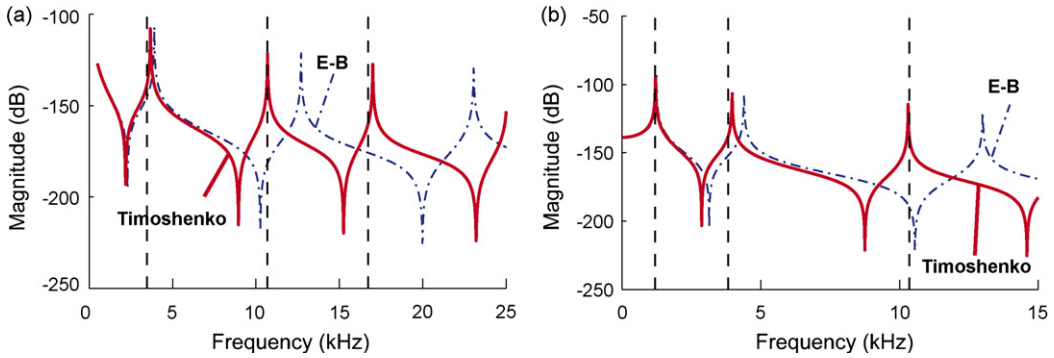

Fig. 7. Comparison of the tool–holder dynamics with E–B and Timoshenko beam models for (a) free-free boundary conditions and (b) for fixed-free boundary conditions. The natural frequencies from the FEM solution are indicated with dashed lines.

Table 2
The differences between the Euler–Bernoulli (E–B)/Timoshenko beam solutions and the FEM solution for the first four bending frequencies (in Hz) for the free-free and fixed-free boundary conditions

	Free-free			Fixed-free		
	FEM	E–B	Timoshenko	FEM	E–B	Timoshenko
Mode 1	3,457	3,900 (12.8%)	3,674 (6.3%)	1,187	1,242 (4.6%)	1,201 (1.2%)
Mode 2	10,688	12,700 (18.8%)	10,692 (0.1%)	3,825	4,394 (14.9%)	3,967 (3.7%)
Mode 3	16,727	23,049 (37.8%)	17,001 (1.6%)	10,357	12,995 (25.5%)	10,297 (0.6%)
Mode 4	24,670	39,895 (61.7%)	25,074 (1.6%)	16,106	23,243 (44.3%)	16,405 (1.9%)

were seen to be 3.8%, 10.5%, 27.2%, and 43.4%, respectively, for the free-free boundary conditions, and 2.9%, 7.3%, 20.3%, and 36.6%, respectively, for the fixed-free boundary conditions. The inaccuracy of the E–B solution would also increase with reduced length-to-diameter ratios. Fig. 9 gives the percent difference (taking the Timoshenko beam solution as the reference) between the E–B and Timoshenko beam solutions for varying length-to-diameter ratio of the tool without changing the other sections of the tool–holder assembly. As expected, when the length-to-diameter ratio of the tool increases, the two solutions approach one another. The differences do not approach zero due to the effect from the other sections of the tool–holder assembly.

4.2. Straight beam approximation

A simplification to the tool–holder model can be attained by approximating the tapered sections of the tool–holder assembly with straight beams of equivalent diameters. To assess the accuracy of such an approximation, Sections 2–4 in Fig. 4 are approximated as straight beams with an average diameter, which is calculated as the arithmetic average of the diameters of the beginning and end of the taper. Using the spectral-Tchebychev technique presented above, and considering each section as a Timoshenko beam, the dynamics of the tool–holder assembly was then modeled. It was seen that the difference between the natural frequencies for the tapered model and the equivalent straight model were very close,

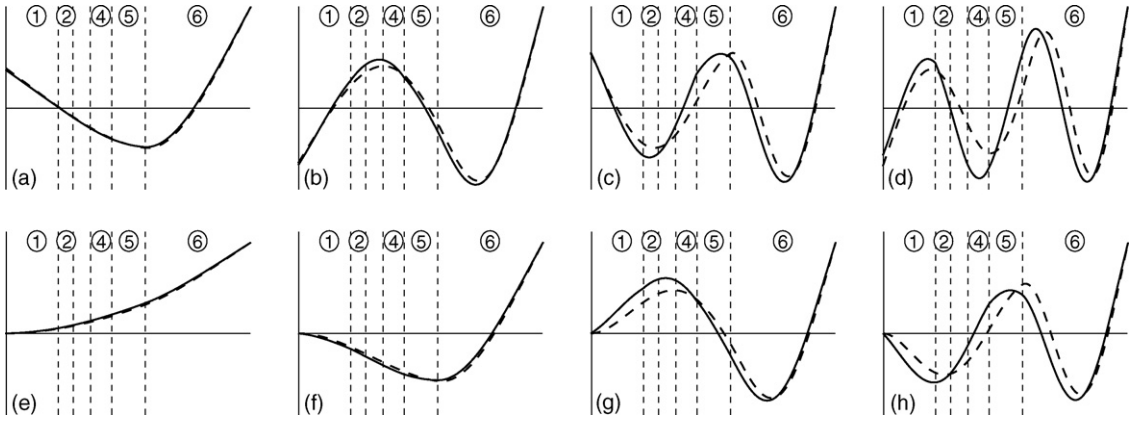

Fig. 8. The first four mode shapes of the tool–holder assembly with E–B (dashed) and Timoshenko beam models for (a)–(d) free-free boundary conditions and (e)–(f) for fixed-free boundary conditions. The encircled numbers correspond to the sections of the assembly.

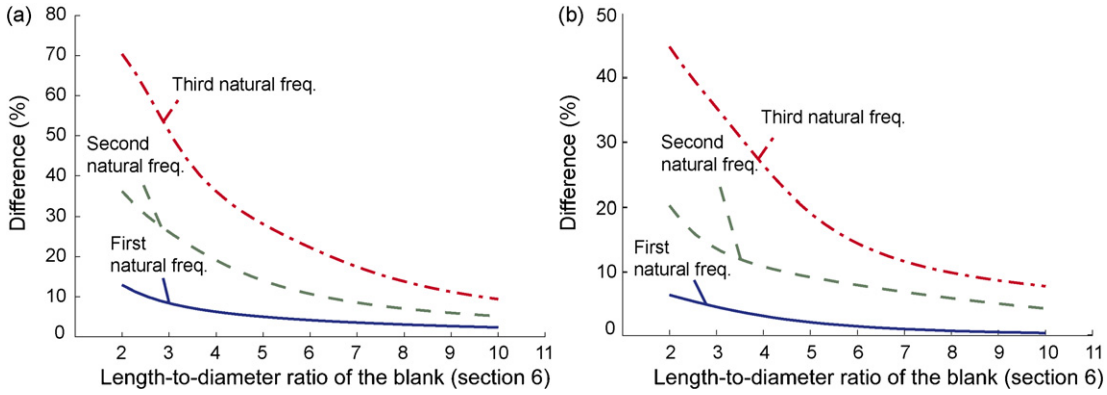

Fig. 9. The percent difference between the natural frequencies of the E–B and Timoshenko solutions with varying length-to-diameter ratio of the tool (Section 6) for (a) free-free and (b) fixed-free boundary conditions (different *y*-scales).

resulting in less than 1% error for the first three modes for both the free-free and fixed-free boundary conditions.

To interpret this observation, the natural frequencies of a tapered and an equivalent straight beam are compared for increasing diameter ratios (ratio of the diameters of the beginning and end sections), while keeping the length of the tapered section (3.33 times the larger diameter) and material properties (steel, see Table 1) constant. In both cases, the beams are modeled using the Timoshenko beam equations, and the spectral-Tchebychev technique was used for the solution. Fig. 10 gives the percent difference between the natural frequencies of the equivalent straight and tapered beams (taking the tapered beam as a reference) for both free-free and fixed-free boundary conditions. As expected, the difference is very small in the vicinity of diameter ratio of 1. However, a the diameter ratio increases, the error from the straight beam assumption rapidly raises. Since the diameter ratios for the tool–holder sections were close to 1 (1.05, 1.07, and 1.12, respectively, for the Sections 3–5), and since only a small portion of the tool–holder was tapered, the error from the straight beam approximation was negligible.

5. Experimental validation

In this section we provide comparisons of tool-point FRF predictions and measurements for three carbide tool blank-tapered shrink fit tool holder combinations clamped in a rolling element bearing, high-speed spindle (HSK-63A holder–spindle interface). As noted in Section 2, there are two primary tasks required for the RCSA procedure. The tool–holder is first modeled as a free-free beam as described in Section 3. This model is then coupled to the spindle–machine receptances using the approach shown in Eq. 2.

In order to determine the spindle–machine receptances (e.g., G_{33} in Eq. (2)) a (cylindrical) standard artifact is inserted in the spindle and direct and cross translational FRFs are measured on the artifact. These translational FRFs are then used to calculate the rotational receptances at the free end of the artifact–spindle–machine assembly. Given this information, the spindle–machine receptances are obtained by the inverse RCSA procedure [18] where the portion of the standard holder beyond the flange is removed in simulation using a rearrangement of Eq. (2) to isolate the spindle–machine receptances (given the receptances of the artifact–spindle–machine and a free-free model of the artifact).

When using this procedure, variations in the artifact direct and cross FRF measurements propagate to the tool-point FRF predictions. Although a rigorous uncertainty analysis for the RCSA procedure has not been completed, repeated artifact measurements were conducted to identify the influence of the FRF data spread on the predictions. For these tests, a laser vibrometer was used to record the direct and cross artifact–spindle–machine response to hammer impacts. Four total data sets were recorded; each data set was composed of 10 groups of 10 repetitions and the artifact was removed from the spindle and replaced prior to collecting the next data set. The removal and replacement of the artifact was completed to incorporate potential dynamic non-repeatability from the HSK-63A clamping procedure.

Fig. 11 shows the mean and frequency-dependent standard deviation (σ) of the real and imaginary parts for the artifact direct FRFs from the first data set (2σ intervals are shown at each frequency). A number of spindle modes are observed, including the

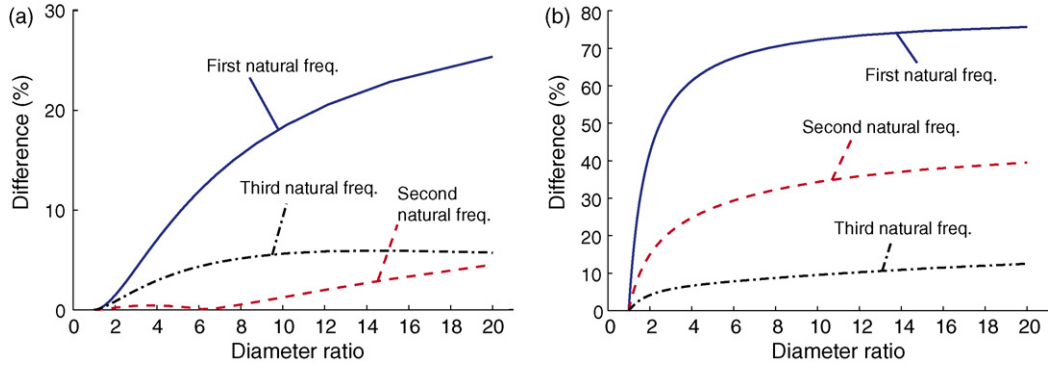

Fig. 10. The percent difference between the natural frequencies of a tapered and an equivalent straight beam for (a) free-free and (b) fixed-free boundary conditions (different *y*-scales).

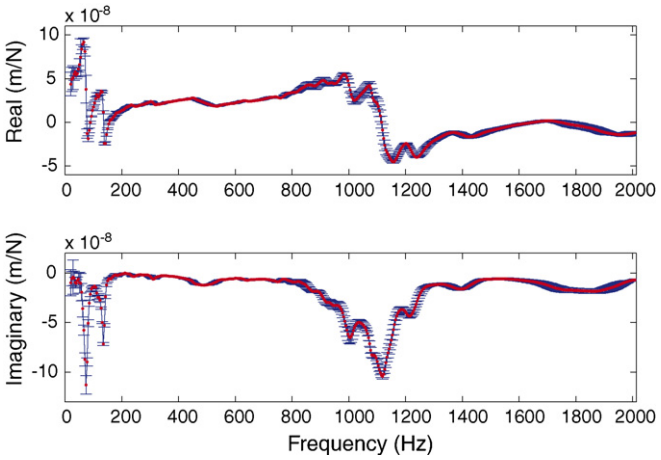

Fig. 11. Mean and 2σ standard deviation intervals for first data set artifact direct FRFs.

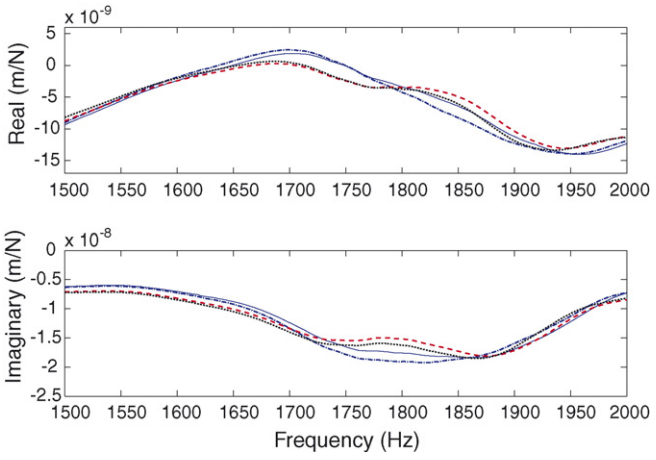

Fig. 13. Means of four data set artifact direct FRFs. Limited frequency range shows differences between selected spindle mode due to removal and re-clamping.

rigid body modes at 74 Hz and 135 Hz. The clamped-free vibration modes of the artifact are well outside the bandwidth of interest. Fig. 12(a) displays the ratio of σ to the corresponding mean FRF magnitude (expressed as a percentage) for the four individual data sets. Higher values are seen in the region of the lightly damped rigid body modes and in the 1500–2000 Hz range. Additionally, the local peaks between data sets are frequency shifted relative to one another and have different amplitudes. If the dynamic system was not changing (from removal and re-clamping of the artifact) and the variation was due solely to impact testing inconsistency, the noise level would be expected to diminish as more data was collected. However, Fig. 12(b) shows that this is not the case. Here, the σ to FRF magnitude ratio was calculated for all four data sets combined and is superimposed on the individual data set results. Clearly, the noise level is not reduced. In fact, the ratio exceeds 100% at 10 Hz (i.e., the standard deviation in all 40 sets of 10 averages is larger than the mean FRF magnitude at this frequency; this point is not shown for scaling purposes).

To emphasize what we believe to be dynamic non-repeatability from one set to the next, Fig. 13 shows the mean of the four data sets for the 1500–2000 Hz frequency range. We do not believe the variations in this spindle mode are caused by hammer impact variations, vibrometer misalignment (note that the vibrometer and spindle–machine were not moved between data sets), or data acquisition/filtering/analysis (the same sampling frequency, filters, and sample length were used for each test). Rather, we believe the variations to be the result of actual changes in the clamped

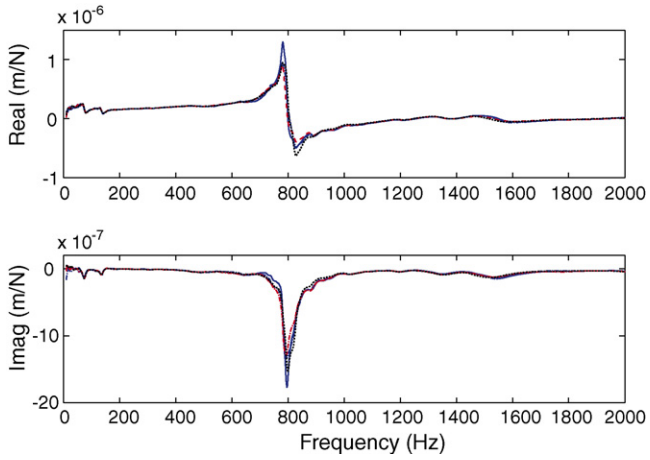

Fig. 14. 77.2-mm overhang tool blank prediction results determined using four artifact data sets.

assembly dynamics. While the differences are small, in the RCSA procedure the direct and cross artifact–spindle–machine receptances are used to first identify the spindle–machine response. This result is then coupled to the tool–holder model to predict the tool-point dynamics.

To explore the influence of artifact FRF variations on this process, each of the four data sets was used to independently determine

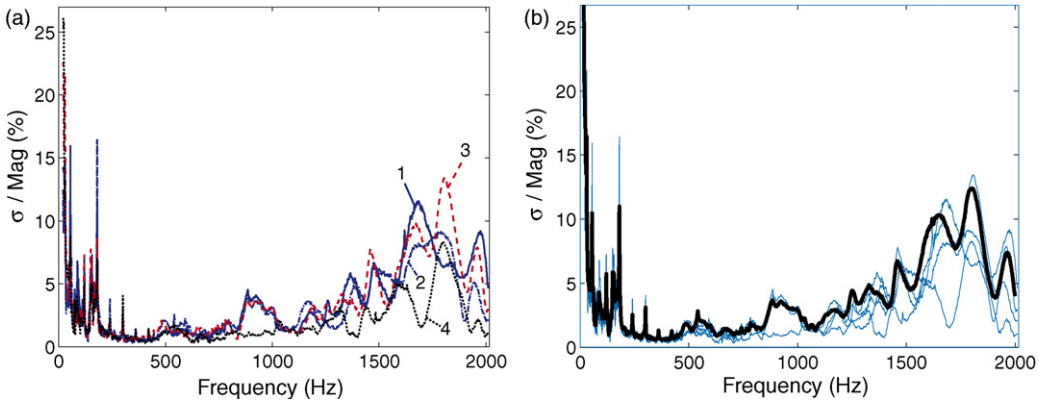

Fig. 12. Ratio of standard deviation, σ, to artifact FRF magnitude (%): (a) for four individual data sets and (b) for all four data sets combined (heavy line) superimposed on individual data sets.

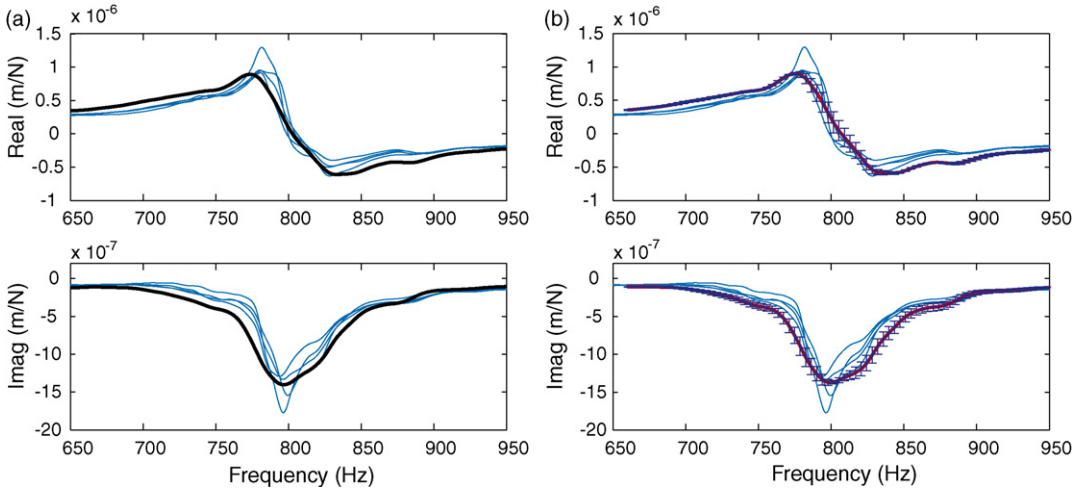

Fig. 15. For the dominant mode of 77.2-mm overhang tool blank-holder (a) comparison between four predictions and measurement (heavy line) and (b) measurement mean with 2σ intervals (five sets of 10 averages) superimposed on four predictions.

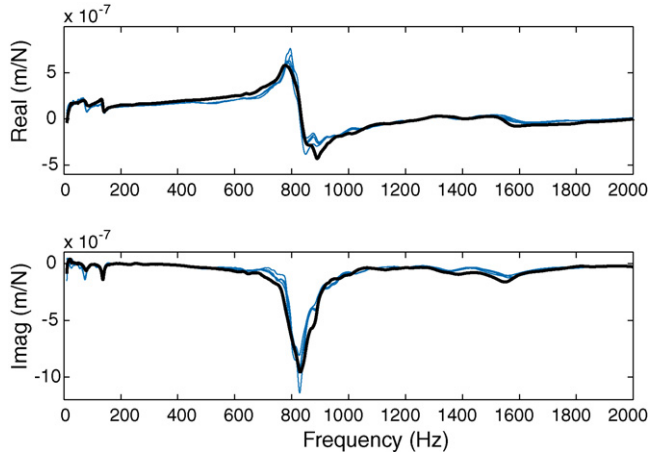

Fig. 16. Comparison between four predictions and measurement (heavy line) for 69.6-mm overhang tool blank-holder.

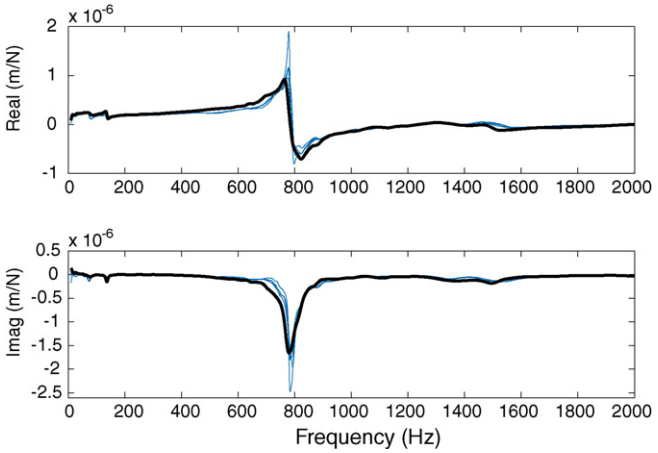

Fig. 17. Comparison between four predictions and measurement (heavy line) 81.2-mm overhang tool blank-holder. The first data set overpredicts the amplitude.

the tool-point response using the same carbide tool blank-tapered shrink fit holder model. The tool–holder dimensions are provided in Fig. 5. The steel holder and carbide tool blank material properties are given in Table 1. The prediction results for the 77.2 mm overhang tool blank are provided in Fig. 14. A comparison between the predictions and measurement for the frequency range from 650 Hz to 950 Hz (to better view the dominant mode) is given in Fig. 15(a). The agreement is good with the four predictions distributed about the measurement result. To qualify this variation, we inserted and removed the tool–holder from the spindle between five subsequent measurements (10 averages for each test). The overall measurement mean and frequency-dependent standard deviation (2σ) are superimposed on the predictions in Fig. 15(b). Although the 2σ intervals do not overlap with the predictions at all frequencies, the disagreement is quite reasonable for the *a priori* predictions.

As a final step, predictions and measurements were completed for two additional tool overhang lengths while using the same tool blank and shrink fit tool–holder. Figs. 16 and 17 display the predictions from the four artifact–spindle–machine data sets for tool overhang lengths of 69.6 mm and 81.2 mm, respectively, superimposed on the tool-point measurement. Good agreement is observed, although the first artifact–spindle–machine data set prediction overestimates the tool-point response amplitude for the 81.2 mm overhang case.

6. Conclusion

An accurate and numerically efficient model of the tool–holder dynamics is derived. The tool–holder model is coupled with the experimentally determined spindle–machine dynamics through RCSA to predict the tool-tip dynamics. The simple, fully parameterized form of the tool–holder model enables tool-tip dynamics predictions for different tool-and-holder selections without the need for extensive experimentation. The model will also enable optimization of tool-tip dynamics by facilitating the selection of optimum tool–holder geometry and/or material. The specific conclusions obtained from this work are as follows:

- Through comparison with an FEM solution, the tool–holder model was shown to be accurate. The Timoshenko beam equation was shown to be more applicable than Euler–Bernoulli solution for modeling tool–holder dynamics.
- The straight beam approximation for modeling the tapered sections of the tool–holder was investigated. Although the approximation was applicable for the considered geometry, it becomes invalid with increasing diameter ratio (taper slope).

- The coupled machine–spindle–tool–holder model was validated through experimentation for three different tool lengths. The variations seen in repeated experiments was concluded to arise from the changes in the clamped assembly dynamics. The model was seen to successfully capture the tool-tip dynamics within the experimental variations.

Acknowledgments

This work was supported by the Philip and Marsha Dowd graduate student fellowship at the Institute of Complex Engineered Systems, Carnegie Mellon University; the Research Initiation Grant from the Society of Manufacturing Engineers #R6001; and by the NSF-CAREER award CMMI-0238019 (Schmitz) and by the NSF-CAREER award CMII-0547534 (Ozdoganlar). The authors wish to thank Dr. Baris Yagci and Dr. Louis Romero for their assistance in the development of the spectral-Tchebychev technique.

References

[1] Schmitz T, Ziegert J. Examination of surface location error due to phasing of cutter vibrations. Precis Eng 1999;23(1):51–62.
[2] Tlusty J. Handbook of high speed machining technology.New York, NY, USA: Chapman and Hall; 1985. p. 140–53.
[3] Kline W, DeVor R, Lindberg J. The prediction of cutting forces in end milling with application to cornering cuts. Int J Mach Tool Des Res 1982;22:7–22.
[4] Sutherland J, DeVor R. An improved method for cutting force and surface error prediction in flexible end milling systems. J Eng Ind, Trans ASME 1986;108:269–79.
[5] Montgomery D, Altintas Y. Mechanism of cutting force and surface generation in dynamic milling. J Eng Ind, Trans ASME 1991;113:160–8.
[6] Altintas Y, Montgomery D, Budak E. Dynamic peripheral milling of flexible structures. J Eng Ind, Trans ASME 1992;114(2):137–45.
[7] Arnold R. Mechanism of tool vibration in cutting of steel. Inst Mech Eng—Proc 1946;154(3):261–76.
[8] Tobias S, Fishwick W. The chatter of lathe tools under orthogonal cutting conditions. Trans ASME 1958;80:1079–85.
[9] Tlusty J, Polacek M. Stability of machine tool against self-excited vibration in machining. Int Prod Eng Res Conf—Proc 1963:465–74.
[10] Merritt H. Theory of self-excited machine-tool chatter: contribution to machine tool chatter research-1. J Eng Ind, Trans ASME 1965;87:447–54.
[11] Smith S, Tlusty J. An overview of modeling and simulation of the milling. J Eng Ind, Trans ASME 1991;113(2):169–75.
[12] Tarng Y, Liao C, Li H. A mechanistic model for prediction of the dynamics of cutting forces in helical end milling. Int J Model Simul 1994;14(2):92–7.
[13] Kline W, DeVor R, Shareef I. The prediction of surface accuracy in end milling. J Eng Ind, Trans ASME 1982;104:272–8.
[14] Schmitz T, Mann B. Closed form solutions for surface location error in milling. Int J Mach Tools Manuf 2006;46:1369–77.
[15] Canning J, Zapata R, Ziegert J, Schmitz T. A comparative study of part error contributors in high-speed machining. In: Proceedings of American society for precision engineering annual meeting, October 15–20. 2006.
[16] Ziegert J, Mize C. The laser ball bar: a new instrument for machine tool metrology. Precis Eng 1994;16(4):259–67.
[17] Schmitz T, Duncan G. Receptance coupling for dynamics prediction of assemblies with coincident neutral axes. J Sound Vibrat 2006;289(4–5):1045–65.
[18] Schmitz T, Duncan G. Three-component receptance coupling substructure analysis for tool point dynamics prediction. J Manuf Sci Eng, Trans ASME 2005;127(4):781–90.
[19] Schmitz T, Davies M, Medicus K, Snyder J. Improving high-speed machining material removal rates by rapid dynamic analysis. CIRP Ann—Manuf Technol 2001;50(1):263–8.
[20] Schmitz T, Davies M, Kennedy M. Tool point frequency response prediction for high-speed machining by RCSA. J Manuf Sci Eng, Trans ASME 2001;123:700–7.
[21] Schmitz T. Predicting high-speed machining dynamics by substructure analysis. CIRP Ann—Manuf Technol 2000;49(1):303–8.
[22] Bishop R, Johnson D. The mechanics of vibration. Cambridge, UK: Cambridge University Press; 1960.
[23] Weaver W, Timoshenko P, Young Jr D. Vibration problems in engineering. 5th edition New York, NY, USA: John Wiley & Sons; 1960.
[24] Yokoyama T. Vibrations of a hanging Timoshenko beam under gravity. J Sound Vibrat 1990;141:245–58.
[25] Hutchinson J. Shear coefficients for Timoshenko beam theory. J Appl Mech, Trans ASME 2001;68(1):87–92.
[26] Filiz S, Ozdoganlar O, Romero L. An analytical model of micro-endmill dynamics in the presence of tool setup errors. In: Proceedings of ASME international conference on manufacturing science and engineering (MSEC) (MSEC2006-21124). 2006.
[27] Gottlieb D, Orszag F. Numerical analysis of spectral methods: theory and applications. SIAM 1977.